

Turbulent boundary layers around wing sections up to

$$Re_c = 1,000,000$$

R. Vinuesa, P. S. Negi, M. Atzori, A. Hanifi, D. S. Henningson
and P. Schlatter

*Linné FLOW Centre, KTH Mechanics, SE-100 44 Stockholm, Sweden
and Swedish e-Science Research Centre (SeRC), Stockholm, Sweden*

Abstract

Reynolds-number effects in the adverse-pressure-gradient (APG) turbulent boundary layer (TBL) developing on the suction side of a NACA4412 wing section are assessed in the present work. To this end, we analyze four cases at Reynolds numbers based on freestream velocity and chord length ranging from $Re_c = 100,000$ to $1,000,000$, all of them with 5° angle of attack. The results of various well-resolved large-eddy simulations, together with the direct numerical simulation by Hosseini *et al.* (*Int. J. Heat Fluid Flow* **61**, 2016) at $Re_c = 400,000$, are used to characterize the effect of Reynolds number on APG TBLs subjected to the same pressure-gradient distribution (defined by the Clauser pressure-gradient parameter β). Comparisons of the wing profiles with zero-pressure-gradient (ZPG) data at matched friction Reynolds numbers reveal that, given the same β distribution, the lower-Reynolds-number boundary layers are more sensitive to pressure-gradient effects. This is reflected in the values of the inner-scaled edge velocity U_e^+ , the shape factor H and the components of the Reynolds-stress tensor in the outer region. This conclusion is supported by the larger wall-normal velocities observed in the lower- Re_c cases. Future extensions of the present work will be aimed at studying the differences in the outer-region energizing mechanisms due to APGs and increasing Reynolds number.

Keywords: turbulence simulation, turbulent boundary layer, pressure gradient, wing section

1. Introduction

Turbulent boundary layers (TBLs) subjected to streamwise pressure gradients (PGs) are relevant to a wide range of industrial applications from diffusers to turbines and wings, and pose a number of open questions regarding their structure and underlying dynamics. A number of studies over the years have aimed at shedding some light on these open questions through various approaches. In the 1950s, Townsend (1956) employed theoretical analyses of the governing equations and concluded that although the only TBL that can be described through self-similar variables is the so-called sink flow (which corresponds to a strongly-accelerated TBL, see for instance the work by Jones et al. (2001)), certain pressure-gradient conditions exhibit self-similarity in their outer region at high Reynolds numbers (Marusic et al., 2010). This includes the widely studied zero-pressure-gradient (ZPG) turbulent boundary layer (Schlatter and Örlü, 2010; Sillero et al., 2014). These so-called near-equilibrium conditions (Dixit and Ramesh, 2009; Bobke et al., 2017) are obtained when the freestream velocity is described in terms of the streamwise coordinate by a power law, given certain restrictions in the exponent (Townsend, 1956). The work by Townsend (1956) was complemented one decade later by Mellor and Gibson (1966), who proposed a theoretical framework to calculate boundary-layer parameters in PG TBLs subjected to a constant pressure-gradient magnitude, represented by a constant value of the Clauser pressure-gradient parameter $\beta = \delta^*/\tau_w dP_e/dx$ (where δ^* is the displacement thickness, τ_w the wall-shear stress and dP_e/dx is the streamwise pressure gradient). Extensive experimental campaigns, such as the ones by Skåre and Krogstad (1994) and Harun et al. (2013), were later undertaken with the aims of obtaining high-Reynolds-number adverse-pressure-gradient (APG) TBLs with constant β (in the case of the former), and further understanding the energizing mechanisms present in favorable-pressure-gradient (FPG) and APG TBLs (in the latter study). The challenges of performing high-fidelity simulations of PG TBLs, especially when it comes to the definition of boundary conditions and to an accurate representation of separated boundary layers, were addressed by Spalart and Watmuff (1993) and Skote and Henningson (2002), respectively. However, and as stated by Monty et al. (2011), the large number of parameters influencing the structure of PG TBLs raises serious difficulties when comparing databases from different experimental or numerical databases. The present work is focused on the analysis of APG effects on TBLs, a flow case that is present on the suction side of wings.

As the boundary layer develops, it encounters a progressively larger resistance manifested in the increased pressure in the streamwise direction. This APG decelerates the boundary layer, increases its wall-normal momentum, and increases its thickness while reducing the wall-shear stress. As a result of the larger boundary-layer thickness the wake parameter in the mean velocity profile increases (Perry et al., 2002; Vinuesa et al., 2014a), and more energetic turbulent structures develop in the outer region (Maciel et al., 2017). The recent work by Bobke et al. (2017) highlights the importance of the flow development in the establishment of an APG TBL, and in particular the streamwise evolution of the Clauser pressure-gradient parameter β . In their study, Bobke et al. (2017) compared different APG TBLs subjected to various $\beta(x)$ distributions, including several flat-plate cases and one APG developing on the suction side of a wing section (Hosseini et al., 2016). Their main conclusion states that the effect of APGs is more prominent in the cases where the boundary layer has been subjected to a stronger pressure gradient for a longer streamwise distance, a conclusion that demonstrates the relevance of accounting for the $\beta(x)$ distribution when assessing pressure-gradient effects on TBLs (Vinuesa et al., 2017c). Along these lines, the numerical studies by Kitsios et al. (2016), Lee (2017) and Bobke et al. (2017) aim at characterizing the effect of APGs on TBLs in cases with a constant pressure-gradient magnitude, *i.e.*, in flat-plate boundary layers exhibiting long regions with constant values of β .

The aim of the present work is to assess the effect of the Reynolds number (Re) on four APG TBLs subjected to the same $\beta(x)$ distribution. In particular, we consider the turbulent flow around a NACA4412 wing section at four Reynolds numbers based on freestream velocity U_∞ and chord length c , ranging from $Re_c = 100,000$ to $1,000,000$. As discussed by Pinkerton (1938), the NACA4412 wing section is characterized by exhibiting a pressure-gradient distribution essentially independent of Re at moderate angles of attack, a fact that makes this particular airfoil a suitable candidate to study Reynolds-number effects on TBLs given a particular pressure-gradient history. A number of numerical studies have been conducted with the aim of characterizing turbulent flows developing around airfoils, including the large-eddy simulations (LESs) of a NACA4412 wing section by Jansen (1996) and the direct numerical simulations (DNSs) of a NACA0012 airfoil by Rodríguez et al. (2013), both at high angles of attack. Other recent LESs include the studies on symmetric airfoils by Wolf et al. (2012) and Sato et al. (2017). However, to the authors' knowledge this is the first numerical study where the

pressure-gradient effects on the turbulent boundary layers are characterized systematically for the same airfoil at several Reynolds numbers.

The present manuscript is organized as follows: the numerical setup setup is described in §2; the results are presented for the boundary layer developing on the suction side of the wing in §3; and finally in §4 a summary of the main conclusions of this study is presented.

2. Computational setup

High-fidelity simulations of the flow around a NACA4412 wing section at various Reynolds numbers were carried out using the spectral-element code Nek5000 (Fischer et al., 2008), developed at the Argonne National Laboratory. In the spectral-element method (SEM) the computational domain is decomposed into elements, where the velocity and pressure fields are expressed in terms of high-order Lagrange interpolants of Legendre polynomials, at the Gauss–Lobatto–Legendre (GLL) quadrature points. In the present work we used the $\mathbb{P}_N - \mathbb{P}_{N-2}$ formulation, which implies that the velocity and pressure fields are expressed in terms of polynomials of order N and $N - 2$, respectively. The time discretization is based on an explicit third-order extrapolation for the nonlinear terms, and an implicit third-order backward differentiation for the viscous ones. The code is written in Fortran 77 and C and the message-passing-interface (MPI) is used for parallelism.

In addition to the DNS at $Re_c = 400,000$ reported by Hosseini et al. (2016) and Vinuesa et al. (2017a), in this work we consider well-resolved LESs at $Re_c = 100,000, 200,000$ and $1,000,000$. The various cases, as well as their respective domain sizes and color codes for the rest of the manuscript, are summarized in Table 1. A two-dimensional slice of the computational domain employed to simulate the $Re_c = 1,000,000$ case is shown in Figure 1 (left), where x , y and z denote the horizontal, vertical and spanwise directions, respectively. In all the cases under consideration the domain is periodic in the spanwise direction, and a width of $L_z = 0.2c$ was considered in the $Re_c = 1,000,000$ wing. In this case, a total of 4.5 million spectral elements was used to discretize the domain with a polynomial order $N = 7$, which amounts to a total of 2.28 billion grid points. As in the DNS by Hosseini et al. (2016), a Dirichlet boundary condition extracted from an initial RANS (Reynolds-Averaged Navier–Stokes) simulation was imposed on all the boundaries except the outflow, where the boundary condition by Dong et al. (2014) was employed. The initial RANS simulation was carried out

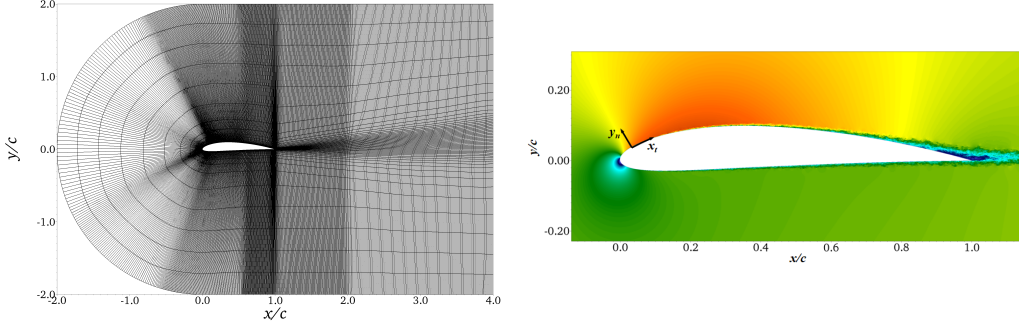


Figure 1: (Left) Two-dimensional slice of the computational domain showing the spectral-element distribution, but not the individual GLL points. (Right) Instantaneous two-dimensional visualization of the horizontal velocity for the $Re_c = 1,000,000$ case. Dark blue represents a horizontal velocity of -0.1 and dark red a value of 2 . The global frame of reference, as well as the local one expressed in the directions tangential and normal to the wing surface, are also shown (note that the z direction is common to both).

Table 1: Summary of wing cases under study.

Re_c	Reference	Type of simulation	L_x/c	L_y/c	L_z/c	Color
100,000	Vinuesa and Schlatter (2017)	LES	5	4	0.1	blue
200,000	Present study	LES	6	4	0.2	red
400,000	Hosseini et al. (2016)	DNS	6.2	2	0.1	green
1,000,000	Present study	LES	6	4	0.2	cyan

with the $k - \omega$ SST (shear-stress transport) model (Menter, 1994) implemented in the commercial software ANSYS Fluent. An angle of attack of 5° was considered in all the Reynolds-number cases. An instantaneous two-dimensional visualization of the horizontal velocity around the wing section at $Re_c = 1,000,000$ is shown in Figure 1 (right), where both the stagnation point and the development of the TBLs on the suction and pressure sides can be observed. A local frame of reference expressed in the directions tangential and normal to the wing surface (*i.e.* given by the coordinates x_t and y_n) is also shown in this figure.

The LES approach is based on a relaxation-term (RT) filter, which provides an additional dissipative force in order to account for the contribution of the smallest, unresolved, turbulent scales (Schlatter et al., 2004). A validation of the method in turbulent channel flows and the flow around a NACA4412 wing section at $Re_c = 400,000$ is given by Negi et al. (2017); note that the same resolution is employed for the $Re_c = 100,000$ and $200,000$

cases. In the $Re_c = 1,000,000$ case, the mesh resolution around the wing follows these guidelines: $\Delta x_t^+ < 27$, $\Delta y_{n,\text{wall}}^+ < 0.96$ and $\Delta z^+ < 13.5$, where the superscript ‘ $+$ ’ denotes scaling in terms of the friction velocity $u_\tau = \sqrt{\tau_w/\rho}$ (with ρ being the fluid density). Regarding the wake, we defined the criterion $\Delta x/\eta < 13.5$, where $\eta = (\nu^3/\varepsilon)^{1/4}$ is the Kolmogorov scale (ν is the fluid kinematic viscosity, and ε the local isotropic dissipation). Note that the overall strategy to build the wing mesh is analogous to the one described by Hosseini et al. (2016) and Negi et al. (2017). The mesh resolutions employed for all the cases under study are summarized in Table 2, where it can be observed that in the $Re_c = 1,000,000$ we employed a coarser resolution than in the two other LES cases due to its high computational cost. In order to assess the accuracy of this coarser resolution, we performed an LES of the $Re_c = 400,000$ case with the guidelines described above, and compared the results with those obtained with DNS (Hosseini et al., 2016). In Figure 2 we compare the inner-scaled mean velocity profile and selected components of the Reynolds-stress tensor at $x_{ss}/c = 0.7$ (note that ss denotes suction side), expressed in the tangential and wall-normal frame of reference, from both simulations. This figure shows an excellent agreement in the mean velocity profile, as well as in the Reynolds-shear stress and in the outer region of the tangential velocity fluctuations. The effect of the reduced resolution is manifested in a small attenuation of the wall-normal and spanwise fluctuations, and in a slight over-prediction of the near-wall peak of $\overline{u_t^2}^+$. However, since the results presented below will be focused on the mean flow, the tangential velocity fluctuations and the Reynolds-shear stress, we consider that the present resolution is adequate for the scope of this study. The averaging times (after discarding initial transients) considered to compute turbulence statistics are reported in Table 2 for all the wing cases in terms of normalized eddy-turnover times. The eddy-turnover time $\text{ETT} = \delta_{99}/u_\tau$ is the characteristic length scale of the large scales, and as discussed by Vinuesa et al. (2016b) it is possible to define a normalized ETT^* , in which the length of the domain in the periodic directions is taken into account. The complete process to compute statistics, which involves averaging in time and in the periodic spanwise direction, as well as tensor rotation to express all the terms in the tangential and wall-normal frame of reference, is described by Hosseini et al. (2016).

In Figure 3 we show instantaneous visualizations showing coherent vortices identified with the λ_2 method (Jeong and Hussain, 1995) in the four

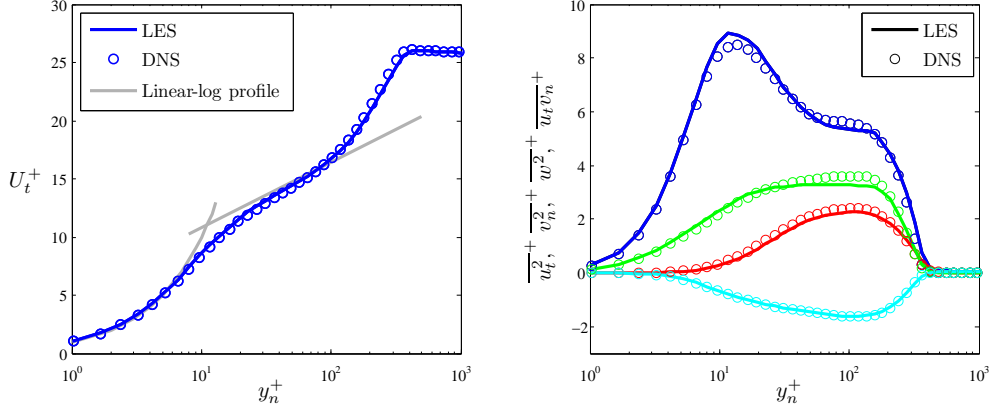


Figure 2: Comparison of $Re_c = 400,000$ DNS by Hosseini et al. (2016) and LES with the resolution employed in the $Re_c = 1,000,000$ case. (Left) Inner-scaled mean velocity profile and (right) components of the Reynolds-stress tensor at $x_{ss}/c = 0.7$.

Table 2: Numerical details of the wing cases under study. The normalized averaging eddy-turnover times ETT_a^* are obtained at $x_{ss}/c = 0.7$.

Re_c	Δx_t^+	$\Delta y_{n,\text{wall}}^+$	Δz^+	Wake	Grid points	ETT_a^*
100,000	18	0.64	9	$\Delta x/\eta < 9$	48.4×10^6	16.2
200,000	18	0.64	9	$\Delta x/\eta < 9$	336×10^6	9.81
400,000	10	0.5	5	$(\Delta x \Delta y \Delta z)^{1/3} < 5\eta$	3.19×10^9	38.3
1,000,000	27	0.96	13.5	$\Delta x/\eta < 13.5$	2.28×10^9	10.5

wing cases under study. Firstly, this figure shows that the present LES approach is adequate to simulate the flow. The boundary layers on the suction and pressure sides were tripped in all the cases using the volume-force method described by Schlatter and Örlü (2012), at $x/c = 0.1$. This figure also illustrates how the scale separation increases with Reynolds number, for a flow case where the geometry is fixed. Whereas the very low $Re_c = 100,000$ case exhibits predominance of hairpin-like structures (Theodorsen, 1952; Adrian, 2007; Schlatter et al., 2014), these progressively become less and less common as Re increases, being essentially absent at $Re_c = 1,000,000$. It is interesting to note how the vortical structures are affected by the pressure-gradient distributions on both sides: on the suction side the progressively stronger APG leads to a thicker boundary layer with larger and more energetic structures, whereas on the pressure side the slight FPG produces a thinner boundary layer with weaker turbulent motions. In particular, the low Re in the $Re_c = 100,000$ case, combined with the slight FPG, lead to partial relaminarization of the boundary layer on the pressure side. The impact of the pressure-gradient distributions on the features of the TBL on the suction side of the wing will be assessed in the next section.

3. Results and discussion

As discussed in the Introduction, the aim of the current study is to investigate the Reynolds-number effects on APG TBLs subjected to the same $\beta(x)$ distribution. In particular, we aim at assessing such effects on the turbulent boundary layer developing on the suction side of a NACA4412 wing section with 5° angle of attack. To this end, we compare the results from the various numerical databases summarized in Table 1, with Re_c ranging from 100,000 to 1,000,000. In Figure 4 (left) we show a sketch comparing the streamwise development of a ZPG and an APG TBL. In the ZPG case, the increase in local Reynolds number in the streamwise direction produces the development of the outer region in the boundary layer, with progressively more energetic large-scale motions (Eitel-Amor et al., 2014; Sillero et al., 2014). This figure also shows that when a streamwise APG is imposed, the wall-normal convection increases significantly, leading to a more pronounced growth of the boundary layer, and consequently to a much more prominent outer region. The APG produces more energetic large-scale motions in the outer region (Harun et al., 2013; Vinuesa et al., 2017a), and as discussed by Maciel et al. (2017) these large structures are taller, shorter in the streamwise direction,

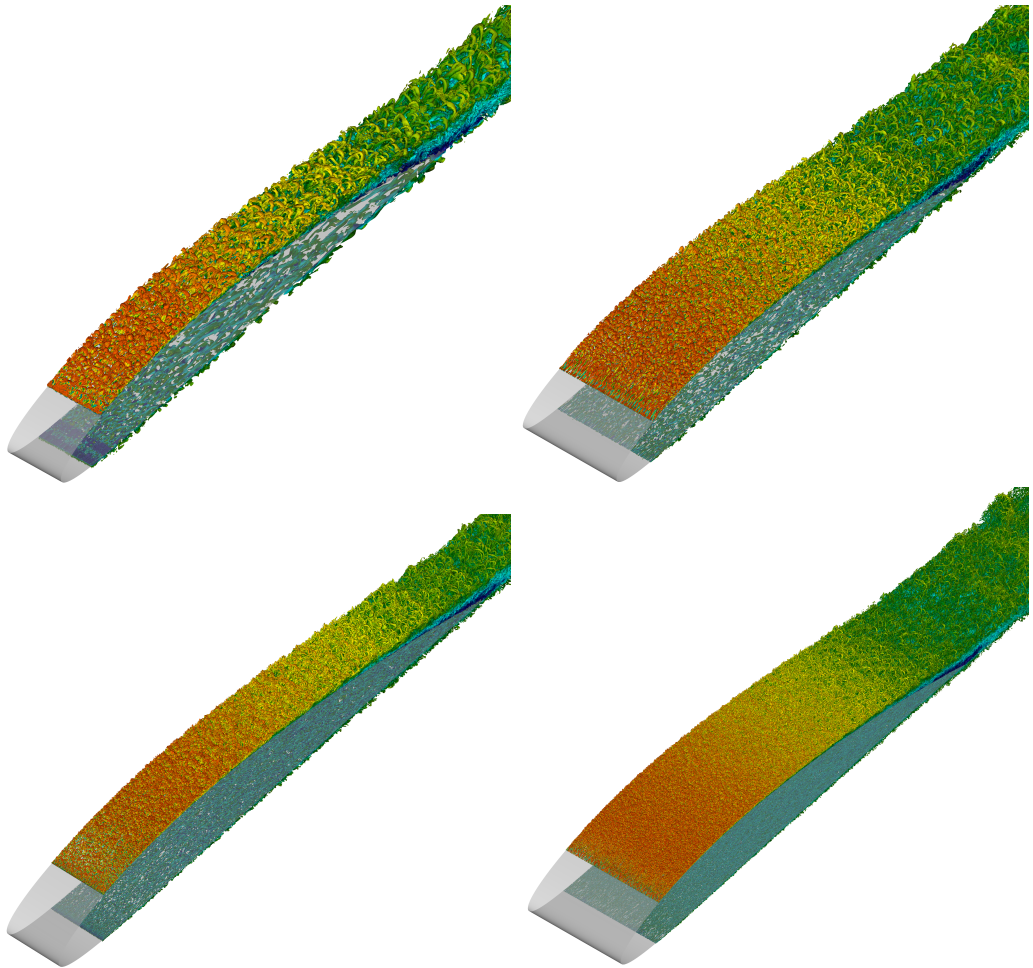


Figure 3: Instantaneous visualizations showing coherent vortices identified using the λ_2 method (Jeong and Hussain, 1995) in the four wing simulations under consideration. An inner-scaled isosurface of $\lambda_2^+ = -10^{-4}$ (based on the value of u_τ at $x_{ss}/c = 0.4$) is shown in all the cases. The structures are colored by the magnitude of the streamwise velocity, where dark blue denotes -0.1 and dark red 2 . The Reynolds number increases from left to right and from top to bottom.

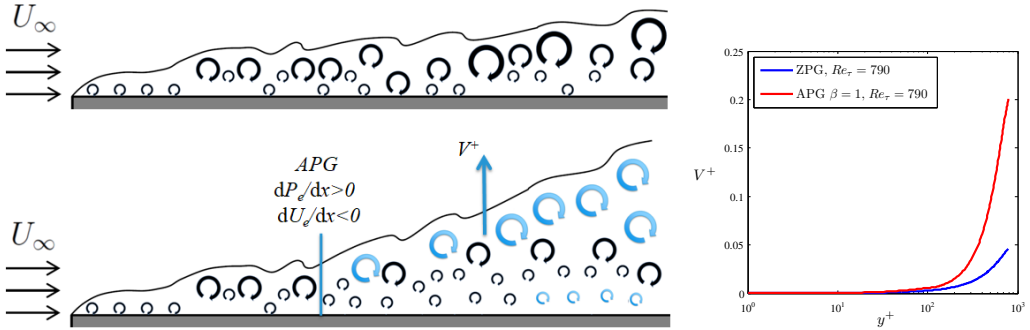


Figure 4: (Left) Sketch showing the streamwise development of (top) a ZPG and (bottom) an APG TBL. In black we represent turbulent structures characteristic of ZPGs, and in blue the ones affected by the wall-normal convection in APG TBLs. (Right) Comparison of inner-scaled wall-normal velocity profile at $Re_\tau = 790$ from a ZPG (Schlatter and Örlü, 2010) and an APG TBL (Bobke et al., 2017). Profiles truncated at the boundary-layer edge.

and they form a larger angle with respect to the wall than their ZPG counterparts due to the effect of the wall-normal convection. As shown in Figure 4 (right), the inner-scaled wall-normal velocity is significantly larger in an APG TBL than in a ZPG, where the former is around 4 times larger than the latter in the boundary-layer edge. Note that in order to avoid the effect of flow history, in Figure 4 (right) we show V^+ profiles for a ZPG TBL (*i.e.* a TBL with a constant value of $\beta = 0$) from the database by Schlatter and Örlü (2010), and for an APG with a constant value of $\beta(x) = 1$ (Bobke et al., 2017), both at the same $Re_\tau = 790$. Note that Re_τ is defined in terms of the boundary-layer thickness and the friction velocity. The impact of the same $\beta(x)$ distribution on TBLs at different Reynolds numbers will be assessed in the rest of this section through the analysis of boundary-layer development, mean velocity and Reynolds-stress profiles.

3.1. Boundary-layer development

In Figure 5 (top) we show the streamwise evolution of the Clauser pressure-gradient parameter β for the TBLs on the suction side of the four wing cases under study. As expected, the three higher- Re boundary layers are subjected to almost identical $\beta(x)$ distributions, with small relative differences only arising beyond $x_{ss}/c > 0.9$. The $Re_c = 100,000$ case shows slightly higher β values throughout the wing chord, especially at $x_{ss}/c = 0.4$, a fact that is connected to the low Reynolds number of this case. Note that all the

boundary layers are subjected to conditions close to zero pressure gradient up to $x_{ss}/c \simeq 0.3$, point after which the value of β increases beyond 0.1. In the next section we will study the velocity profiles at $x_{ss}/c = 0.4$ and 0.7, in which the pressure-gradient magnitude is moderate ($\beta \simeq 0.6$) and strong ($\beta \simeq 2$), respectively. Although the value of β increases throughout the whole suction side of the wing, an inflection point is observed at $x_{ss}/c = 0.4$, which is the point of maximum thickness in the NACA4412 airfoil. Beyond this point, the rate of change of β increases significantly with x , a fact that is explained by the progressive reduction in airfoil thickness, which produces a larger increase in streamwise adverse pressure gradient.

In Figure 5 (middle) and (bottom) we show the streamwise evolution of the Reynolds number based on momentum thickness Re_θ , and the friction Reynolds number $Re_\tau = \delta_{99} u_\tau / \nu$, respectively. Note that δ_{99} is the 99% boundary-layer thickness, which was determined following the method described by Vinuesa et al. (2016a) for pressure-gradient TBLs. The Re_θ trends increase monotonically in the four boundary layers, due to the fact that both Reynolds number and APG promote the increase of the boundary-layer thickness. In particular, the thickening experienced by the TBLs due to the APG significantly increases Re_θ in all the cases, with maximum values of $Re_\theta = 1,050, 1,700, 2,800$ and $6,000$ (from low to high Re_c), all of them observed close to the trailing edge. Regarding the friction Reynolds number, note that in all the boundary-layer cases the maximum is located at $x_{ss}/c \simeq 0.8$, and not close to the trailing edge as in Re_θ . This is due to the fact that, although the APG increases the boundary-layer thickness, it also decreases the wall-shear stress; thus, the very strong APGs beyond $x_{ss}/c \simeq 0.8$ (where $\beta \simeq 4.5$ in the three higher- Re cases) produce a larger reduction in u_τ than the increase in δ_{99} . The maximum Re_τ values are 173, 238, 373 and 707 in the various wing cases. The decreasing trend in the $Re_c = 100,000$ case up to $x_{ss} \simeq 0.4$ is associated to the very low Reynolds number of this cases, and will be further discussed below. Moreover, the $Re_c = 400,000$ case shows a trend different to that of the other cases up to $x_{ss}/c \simeq 0.2$, a fact that is explained by the volume-force tripping at $x_{ss}/c = 0.1$. In the rest of cases described in this study, the tripping parameters were chosen following the work by Schlatter and Örlü (2012) in ZPG TBLs; however, in the $Re_c = 400,000$ wing the number of modes in the spanwise direction was larger than in Schlatter and Örlü (2012), a fact that produces a long intermittent region in the post-transitional regime. Nevertheless, the boundary layers can be considered to be essentially independent of the tripping beyond

$x_{ss}/c \simeq 0.2$ (Vinuesa et al., 2016a).

The skin-friction coefficient $C_f = 2(u_\tau/U_e)^2$ (where U_e is the velocity at the boundary-layer edge) and the shape factor $H = \delta^*/\theta$ are shown, as a function of the streamwise position on the suction side of the wing, in Figure 6. As in the Re_τ curves shown in Figure 5, the $Re_c = 400,000$ case shows a different behavior in C_f upstream of $x_{ss} \simeq 0.2$. However, beyond this point the effect of the higher number of modes used in the tripping appears to be absent. It can be observed that the $Re_c = 200,000$ curve is slightly above the one of the $Re_c = 400,000$ wing, which in turn also exhibits larger values than that of the $Re_c = 1,000,000$. Interestingly, the differences between these cases are significantly reduced beyond $x_{ss}/c \simeq 0.9$. Since these three boundary layers are subjected to the same $\beta(x)$ distribution, it can be argued that the differences between the various curves are due to Reynolds-number effects, a fact that is consistent with what is observed in ZPG TBLs since C_f decreases with Re . Interestingly, the effect of Reynolds number becomes essentially negligible beyond $x_{ss}/c \simeq 0.9$, where the very strong APG conditions (with a value of $\beta \simeq 14$ at $x_{ss}/c = 0.9$) define the state of the boundary layer. Regarding the shape factor, note that APG and Reynolds number have opposite effects on a TBL: whereas the former increases H (due to the thickening of the boundary layer caused by the increased wall-normal momentum), the latter decreases the shape factor. This can also be observed in Figure 6 (bottom), where the H curve from the $Re_c = 1,000,000$ is below the one from the $Re_c = 400,000$ (which also exhibits the effect of the different tripping up to $x_{ss}/c \simeq 0.2$) throughout the whole suction side of the wing. The $Re_c = 200,000$ curve is above the 400,000 one. Note that, since the three boundary layers are subjected to essentially the same pressure-gradient effects, the lower values of H are produced by the higher Reynolds number, again consistent with what is observed in ZPGs.

Figure 6 also shows that the $Re_c = 100,000$ exhibits a different trend in C_f and H , compared to the ones observed at higher Reynolds numbers. In particular, a steep decrease in skin-friction coefficient is present up to $x_{ss}/c \simeq 0.4$, followed by an increase up to $x_{ss}/c \simeq 0.6$, point after which the C_f experiences an evolution close to the higher- Re cases. Regarding the shape factor, a more pronounced growth is present up to $x_{ss}/c \simeq 0.4$, followed by a slight decrease, and by another region of increasing H beyond $x_{ss}/c \simeq 0.6$. Despite the different behavior in both quantities, which resembles that of a laminar boundary layer experiencing transition up to $x_{ss}/c \simeq 0.4$, note that the flow exhibits coherent vortical structures characteristic of TBLs in

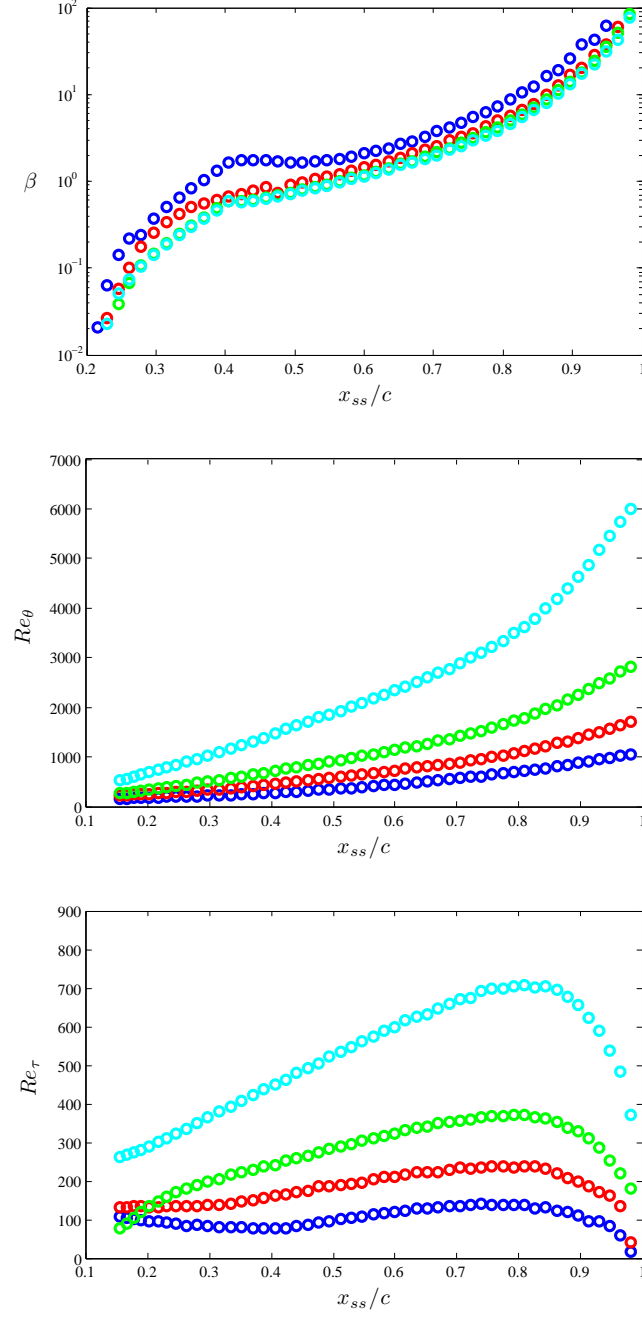


Figure 5: Streamwise evolution of (top) the Clauser pressure-gradient parameter β , (middle) the Reynolds number based on momentum thickness Re_θ and (bottom) the friction Reynolds number Re_τ on the suction side of the wing. The colors correspond to the cases summarized in Table 1.

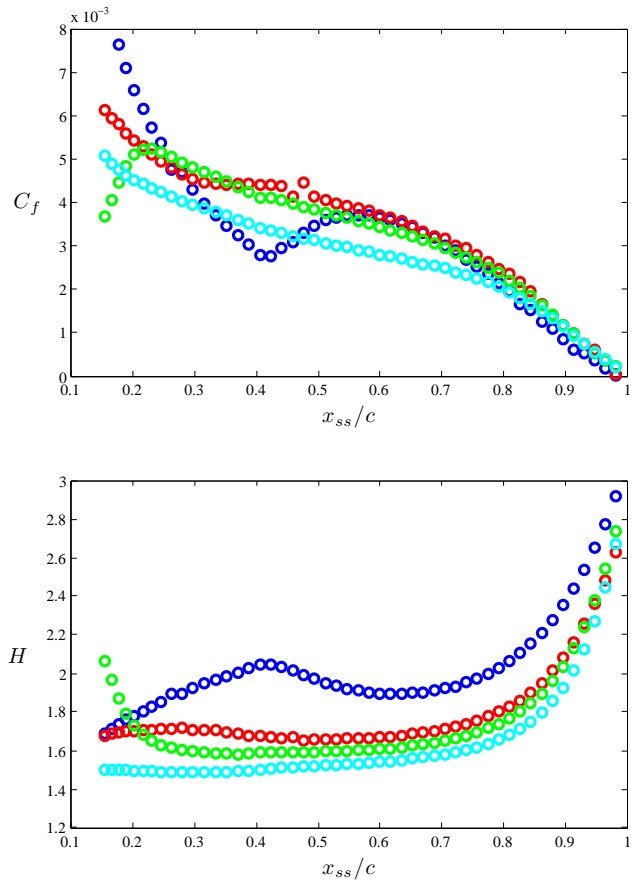


Figure 6: Streamwise evolution of (top) the skin-friction coefficient C_f and (bottom) the shape factor H on the suction side of the wing. The colors correspond to the cases summarized in Table 1.

this region, as observed in the visualization from Figure 3. In Figure 7 (left) we show the streamwise evolution of the wall-shear stress τ_w from the $Re_c = 100,000$ case, compared to that of an additional simulation performed with the same setup, with one difference: in the latter, the volume-force tripping was disabled. This figure shows that the τ_w curves from both cases are identical up to $x_{ss}/c = 0.1$, *i.e.* the location where the volume-force tripping is active in one of them. After the peak in τ_w , the tripped case shows values of wall-shear stress higher than those in the case without tripping, indicating that this portion of the flow is indeed not laminar. The case without tripping exhibits negative values of τ_w beyond $x/c \simeq 0.3$, a fact that indicates that the boundary layer separates at this location. Natural transition is observed at $x_{ss}/c \simeq 0.65$, and beyond $x_{ss}/c \simeq 0.7$ the boundary layer reattaches, exhibiting larger wall-shear stress values than the tripped case. It can then be argued that the very low Reynolds number in the tripped configuration does not exhibit sufficient scale separation for a complete turbulent state to develop, and only after $x_{ss}/c \simeq 0.4$, where the strongest APG effects are present, the boundary layer starts to converge towards the completely-turbulent state. In Figure 7 we show the evolution of the Reynolds number based on displacement thickness Re_{δ^*} , where the typical value of $Re_{\delta^*} = 450$ employed as inflow condition in our flat-plate boundary-layer simulations (Eitel-Amor et al., 2014; Bobke et al., 2017), before the volume-force tripping, is highlighted. This figure indicates that the tripped $Re_c = 100,000$ case only reaches $Re_{\delta^*} = 450$ at $x_{ss}/c \simeq 0.35$, a fact that suggests that this case is not in a completely-turbulent state for a significant part of the streamwise extent, therefore justifying the different behavior compared to the higher- Re wings.

3.2. Inner-scaled mean velocity and Reynolds-stress profiles

Figure 8 (top) shows the inner-scaled mean velocity profiles at $x_{ss}/c = 0.4$ and 0.7 for the four wing cases, where U_t^+ is the inner-scaled mean velocity in the direction tangential to the wing surface, whereas y_n^+ is the inner-scaled wall-normal coordinate. In Tables 3 and 4 we show the boundary-layer parameters at those two streamwise locations, together with the ones from ZPG TBL profiles (Schlatter and Örlü, 2010) at approximately matching Re_τ values. Note that the lowest Re_τ in the DNS database by Schlatter and Örlü (2010) is 252, which implies that at $x_{ss}/c = 0.4$ the two lower- Re wings do not have a matching ZPG profile, whereas at $x_{ss}/c = 0.7$ only the $Re_c = 100,000$ case is left without a matching ZPG case. These tables

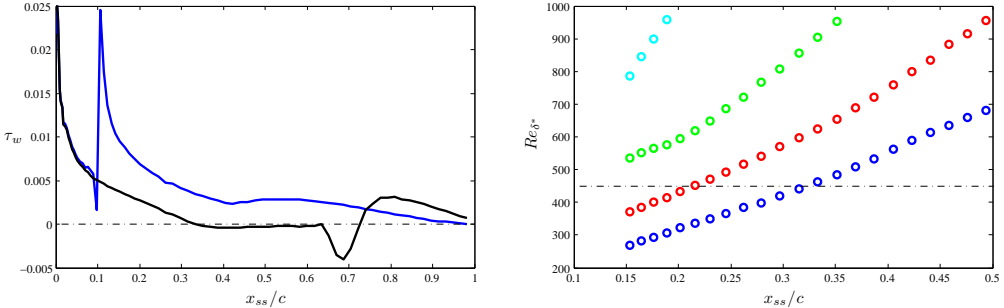


Figure 7: (Left) Streamwise evolution of the wall-shear stress on the suction side of the wing at $Re_c = 100,000$, where — corresponds to the tripped case from Table 1 and — to a case without tripping. The zero-wall-shear-stress level is denoted by - - - . (Right) Streamwise evolution of the Reynolds number based on displacement thickness on the suction side of the wing, where colors correspond to the cases summarized in Table 1. Here - - - denotes the value $Re_{\delta^*} = 450$.

also reflect that, except the lowest- Re case (which as discussed above is not completely turbulent), all the wing profiles are subjected to the same values of $\beta \simeq 0.6$ and 2 at $x_{ss}/c = 0.4$, and 0.7. The mean-flow comparisons between wing and APG are performed at approximately matching values of Re_{τ} , with the aim of assessing the effect of the APG with respect to the baseline ZPG case. Although this comparison can be done by matching several quantities (such as Re_{δ^*} or Re_{θ}), in the present work we fixed Re_{τ} as in the studies by Monty et al. (2011), Harun et al. (2013) or Bobke et al. (2017). Note that by fixing Re_{τ} we compare two boundary layers which essentially exhibit the same range of spatial scales, but subjected to different pressure-gradient conditions. The first noticeable conclusion is the more prominent wakes present in the APG TBLs compared with the corresponding ZPG TBLs at the same Re_{τ} , which is due to the lower skin-friction coefficient caused by the increased wall-normal convection. In addition to this, the shape factor is larger in APGs than in the corresponding ZPG boundary layers (as noted in Tables 3 and 4), a fact that is connected to the boundary-layer thickening, also induced by the APG. Note that the $Re_c = 100,000$ profile at $x_{ss}/c = 0.4$ is not in a completely turbulent state, as discussed above, which is manifested in the mean velocity profile as well. A first step towards characterizing the effect of Re in the TBLs subjected to this particular $\beta(x)$ distribution (see Figure 5 (top)) is to observe the evolution of U_e^+ and H over the given Re_{τ} range in the ZPG and APG cases. In Figure 8 (bottom), we show the

Table 3: Boundary-layer parameters at $x_{ss}/c = 0.4$ for the various wing cases under study. W1, W2, W4 and W10 denote the wing cases at progressively higher Re_c . ZPG4 and ZPG10 denote the DNS ZPG TBL cases (Schlatter and Örlü, 2010) approximately matching the Re_τ values of the wing profiles at $Re_c = 400,000$ and $1,000,000$, respectively.

Parameter	W1	W2	W4	W10	ZPG4	ZPG10
β	1.6	0.67	0.6	0.58	$\simeq 0$	$\simeq 0$
Re_τ	76	161	242	449	252	492
Re_θ	276	453	712	1,465	678	1,421
C_f	2.8×10^{-3}	4.4×10^{-3}	4.1×10^{-3}	3.4×10^{-3}	4.8×10^{-3}	3.9×10^{-3}
H	2.04	1.67	1.59	1.50	1.47	1.43

ratios $\Phi_{U_e^+}$ and Φ_H as a function of Re_c , at the two streamwise positions under consideration. These ratios are defined as the value of U_e^+ (or H) from the TBL on the wing at a certain Re_c and x_{ss} , divided by the same quantity in a ZPG TBL with the same Re_τ . As noted above, both U_e^+ and H are larger in APGs, thus the ratios $\Phi_{U_e^+}$ and Φ_H have values larger than 1, ranging from 1.07 and 1.23 in the case of $\Phi_{U_e^+}$, and from 1.05 to 1.16 for Φ_H depending on the case under consideration. Interestingly, the two indicators exhibit a decreasing trend with Re_c at both streamwise positions, a fact that indicates that the values of U_e^+ and H are more severely affected by the pressure gradient at lower Reynolds numbers, when all the TBLs were subjected to the same $\beta(x)$ distribution. Additional support for this claim can be found in the mean velocity profiles at $y_n^+ \simeq 25$, where the ZPG cases and the wing at $Re_c = 1,000,000$ exhibit almost identical values of the inner-scaled velocity U_t^+ , but the lower- Re wings show values below these in the two streamwise positions. Lower velocities in the buffer layer with respect to the ZPG are associated with strong effects of the APG, as documented for instance by Spalart and Watmuff (1993) or Bobke et al. (2017). This is another indication of the fact that the effect of the APG is more pronounced at lower Re .

As discussed by Harun et al. (2013) or Bobke et al. (2017), the APG energizes the outer region of the boundary layer, producing more energetic turbulent structures. This effect is also observed when increasing the Reynolds number in a ZPG TBL, since as the boundary layer develops the outer region exhibits more energetic structures as shown for instance in the experiments by Hutchins and Marusic (2007) and the numerical simulations by Eitel-Amor et al. (2014). However, the mean velocity profiles shown in Figure 8 suggest that there may be differences in the way that this energizing pro-

Table 4: Boundary-layer parameters at $x_{ss}/c = 0.7$ for the various wing cases under study. W1, W2, W4 and W10 denote the wing cases at progressively higher Re_c . ZPG2, ZPG4 and ZPG10 denote the DNS ZPG TBL cases (Schlatter and Örlü, 2010) approximately matching the Re_τ values of the wing profiles at $Re_c = 200,000, 400,000$ and $1,000,000$, respectively.

Parameter	W1	W2	W4	W10	ZPG2	ZPG4	ZPG10
β	3.7	2.51	2.1	2.0	$\simeq 0$	$\simeq 0$	$\simeq 0$
Re_τ	136	234	356	671	252	359	671
Re_θ	566	895	1,415	2,877	678	1,007	2,001
C_f	3.0×10^{-3}	3.1×10^{-3}	2.9×10^{-3}	2.5×10^{-3}	4.8×10^{-3}	4.3×10^{-3}	3.5×10^{-3}
H	1.92	1.72	1.64	1.58	1.47	1.45	1.41

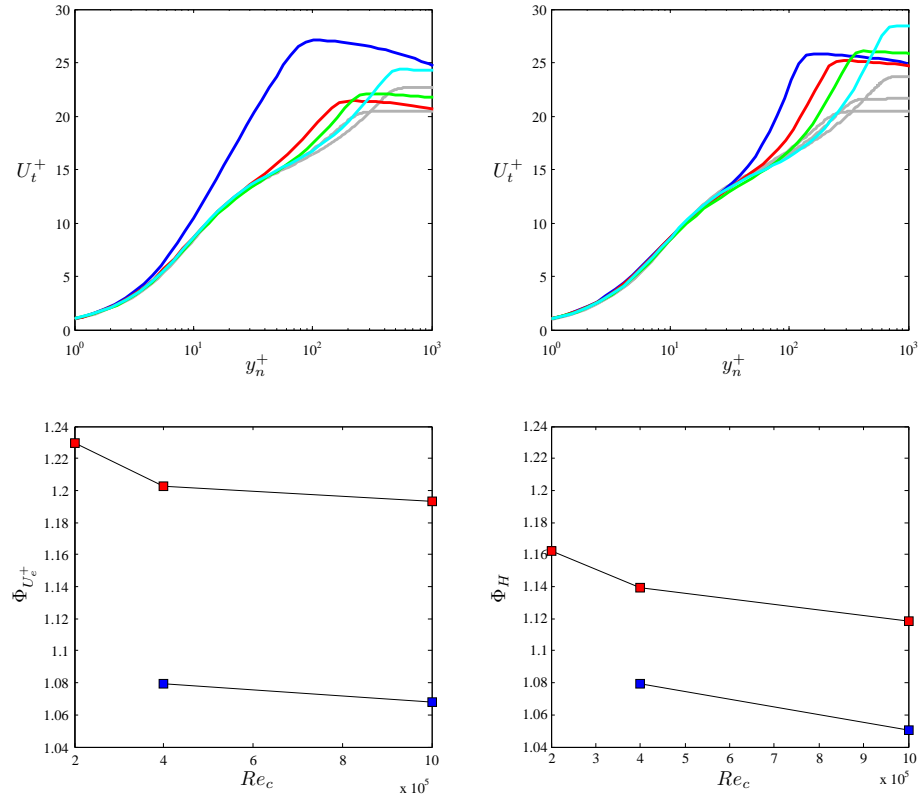


Figure 8: Inner-scaled tangential mean velocity profiles at (top-left) $x_{ss}/c = 0.4$ and (top-right) $x_{ss}/c = 0.7$, for the four wing cases under study, compared with the DNS results of ZPG TBL by Schlatter and Örlü (2010) at approximately matching Re_τ values. Colors from wing cases as in Table 1, and — denotes ZPG TBL data. Ratio of (bottom-left) U_e^+ and (bottom-right) H , between wing and ZPG at approximately matching Re_τ . Here (■) and (■) denote ratios at $x_{ss}/c = 0.4$ and 0.7, respectively.

cess takes place, since the evolution of the mean flow parameters with Reynolds number is not the same in the $\beta = 0$ (ZPG) as in the APG cases. In particular, it is interesting to note that at low Reynolds numbers the effect of the APG appears to be more prominent than at higher Re . This was pointed out in the preliminary work by Vinuesa et al. (2017b), as well as in the experimental study by Sanmiguel Vila et al. (2017). In the latter, the lower- Re numerical data exhibited more pronounced APG features than the measurements. Large-scale energetic motions develop in ZPG TBLs at increasing Reynolds number together with the development of the outer region of the boundary layer. The present results suggest that such development of the outer region takes place in a different way when an APG is present, a fact that is closely connected to the much larger wall-normal convection in APGs, as also illustrated schematically in Figure 4. In APG TBLs there are two complementing mechanisms responsible for the development of the boundary-layer outer region, namely due to β and due to Re . In order to further analyze the differences between these mechanisms, several components of the Reynolds-stress tensor are shown for the two wing cases at $x_{ss}/c = 0.4$ and 0.7 in Figure 9. Note that we also show the Reynolds-stress profiles from the ZPG DNS by Schlatter and Örlü (2010) at approximately matching Re_τ values (as in Figure 8) for comparison. The first important conclusion that can be drawn from Figure 9 is the fact that all the components of the Reynolds-stress tensor under study exhibit a more energetic outer region in comparison with ZPG TBLs, as discussed for instance by Kitsios et al. (2016) or Bobke et al. (2017). As in the case of the mean velocity profiles, the $Re_c = 100,000$ case exhibits different trends than the ones from the higher- Re cases, which again confirms that the boundary layer is not completely turbulent. Focusing on the $\overline{u_t^2}^+$ and $\overline{u_t v_n}^+$ profiles, it can be noted that the APG TBLs exhibit a much more energetic outer region than the corresponding ZPG cases at the same Re_τ . This is further quantified in Figure 9 (bottom), where the ratios $\Phi_{\overline{u_t^2}^+}$ and $\Phi_{\overline{u_t v_n}^+}$ are shown for the various wing cases, at the two locations under consideration. In this figure, the ratios are defined as the wing values of the tangential velocity fluctuation and the Reynolds shear-stress profiles, at $y_n/\delta_{99} = 0.2$, divided by the ones from the ZPG profile at approximately matching Re_τ . This wall-normal location indicates the end of the overlap region in ZPG TBLs for $Re_\theta < 6,000$ (Vinuesa et al., 2014b), but evaluating these ratios in other locations within the overlap layer would yield qualitatively similar trends. As in the case of

the mean flow, these indicators are larger than 1 (which implies that the APG TBLs exhibit more energetic outer regions and higher Reynolds-shear stresses than the corresponding ZPGs), where $\Phi_{\bar{u}_t^2+}$ ranges from 1.13 to 1.82, and $\Phi_{\bar{u}_t \bar{v}_n +}$ from 1.23 to 2.01. The decreasing trends with Re of these indicators reveal that lower- Re TBLs exhibit a higher energy concentration in the outer region than higher- Re cases. Moreover, this also reflects the fact that at lower Reynolds numbers the TBLs are more sensitive to APG effects than the higher- Re cases, a conclusion in agreement to what was observed in the mean flow. This is a very relevant result, since it shows not only that the energizing mechanisms of the outer region in the boundary layer are different when they are connected to APG than when they are associated to Re , but also that lower- Re TBLs are more sensitive to pressure-gradient effects than high- Re ones. In particular, the tangential velocity fluctuation profiles show larger outer-region values in the lower- Re cases: the values of \bar{u}_t^2+ at $y_n/\delta_{99} = 0.2$ are, for the wings at $Re_c = 200,000, 400,000$ and $1,000,000$, 5.8, 5.6 and 5.0, respectively. This is a manifestation of the more prominent energy accumulation in the large-scale motions at low Re than in the high- Re APG boundary layers.

The mean-flow and Reynolds-stress-tensor statistics presented above indicate that, given the same streamwise evolution of β , low-Reynolds-number boundary layers are more significantly affected by the pressure gradient. It is possible to present an additional argument supporting this claim by analyzing the wall-normal velocity distributions since, as illustrated in Figure 4, an APG increases the wall-normal convection throughout the boundary layer. In Figure 10 (left) we compare the inner-scaled wall-normal velocity distributions form the various wing cases, all of them at $x_{ss}/c = 0.7$. As expected, the lower- Re wings exhibit larger V_n^+ values than the higher- Re cases across the whole boundary layer, a fact that is consistent with the stronger APG effects at low Reynolds numbers. This analysis is extended to the whole streamwise extent of the wing in Figure 10 (right), where the ratio of the wall-normal velocity at the boundary-layer edge V_e^+ for the three lower- Re wings is calculated, at each x_{ss} position, with respect to the value of the case with $Re_c = 1,000,000$. Note that this figure shows slight oscillations due to the difficulties in determining the boundary-layer edge in PG TBLs (Vinuesa et al., 2016a), which are produced by the fact that the tangential velocity is not constant for $y_n > \delta_{99}$. In any case, this figure shows that the $Re_c = 400,000$ wing exhibits V_e^+ values around 10% larger than

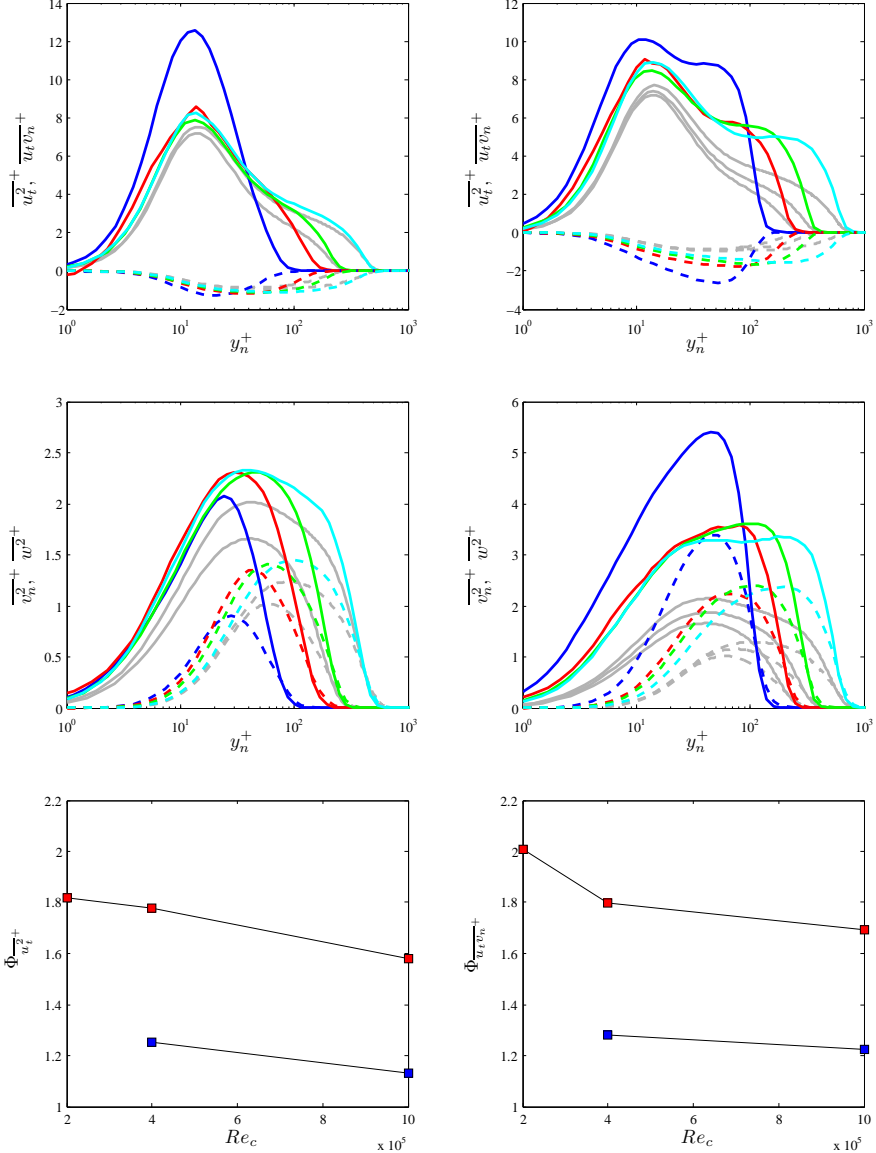


Figure 9: Selected inner-scaled components of the Reynolds-stress tensor at (top-left, middle-left) $x_{ss}/c = 0.4$ and (top-right, middle-right) $x_{ss}/c = 0.7$, for the four wing cases under study, compared with the DNS results of ZPG TBL by Schlatter and Örlü (2010) at approximately matching Re_τ values. Wall-normal profiles of (top panels) tangential velocity fluctuations (solid) and Reynolds-shear stress (dashed), and (middle panels) wall-normal (dashed) and spanwise (solid) velocity fluctuations are shown. Colors from wing cases as in Table 1, and — denotes ZPG TBL data. Ratio of (bottom-left) $\overline{u_t^2}^+$ and (bottom-right) $\overline{u_t v_n^+}$ between wing and ZPG at $y_n/\delta_{99} \simeq 0.2$. Here (■) and (■) denote ratios at $x_{ss}/c = 0.4$ and 0.7, respectively.

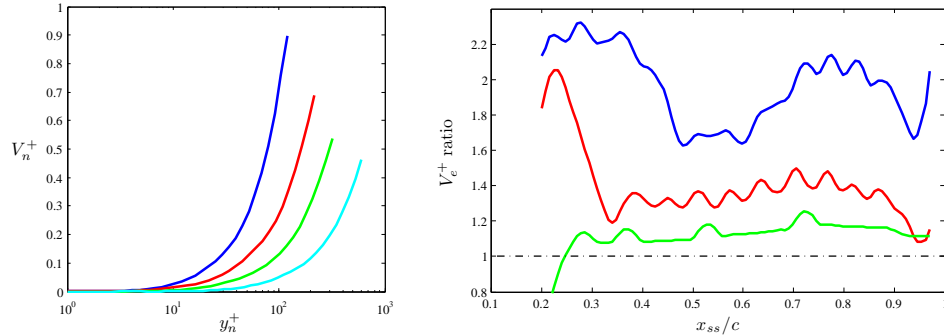


Figure 10: (Left) Inner-scaled wall-normal velocity profiles at $x_{ss}/c = 0.7$, truncated at the boundary-layer edge. (Right) Streamwise evolution of the ratio of the inner-scaled wall-normal edge velocity from the lower- Re wing cases and the one with $Re_c = 1,000,000$. $--$ Denotes a ratio of 1, and colors from wing cases are as in Table 1.

those of the $Re_c = 1,000,000$ case, and in the 200,000 case the values are around 30% higher. The trend associated to the 100,000 wing also shows the change in trend around $x_{ss}/c \simeq 0.4$ discussed above, which is associated to low-Reynolds-number effects. Nevertheless, the higher wall-normal velocities exhibited by the $Re_c = 200,000$ and 400,000 cases imply that the development of the outer layer has been more significantly affected by the APG, thus producing more energetic large-scale motions as evident from the turbulence statistics.

4. Summary and conclusions

The present study is aimed at further understanding the mechanisms responsible for the development of the outer region of TBLs and for the energizing of the large-scale motions, as well as their connection with APGs and increasing Reynolds number. To this end, we analyzed the turbulent boundary layers developing around a NACA4412 wing section at Re_c values from 100,000 to 1,000,000, all of them with 5° angle of attack. All the simulations were performed with the spectral-element code Nek5000, using a setup similar to the one employed by Hosseini et al. (2016) and Vinuesa et al. (2017a) to perform a DNS of the same flow case at $Re_c = 400,000$. The boundary layers developing on the suction side of the wing sections, for $Re_c \geq 200,000$, are subjected to essentially the same streamwise Clauser pressure-gradient distribution $\beta(x)$, a fact that allows to characterize the

effect of the Reynolds number in APG TBLs subjected to exactly the same pressure-gradient history. Note that this study complements the one by Bobke et al. (2017) on flat-plate APG TBLs, in which the effect of different $\beta(x)$ distributions over similar Reynolds-number ranges was assessed.

As a TBL develops, the increasing Reynolds number produces a more energetic outer region, a fact that is manifested in the Reynolds-stress tensor profiles. On the other hand, an APG also produces more energetic large-scale motions in the outer region of the boundary layer due to the increased wall-normal convection associated to it. Our results indicate that the skin-friction curve from the wing at $Re_c = 1,000,000$ is below the ones at lower Reynolds numbers (up to around $x_{ss}/c \simeq 0.9$), a fact that is consistent with the well-known effect of Reynolds number in ZPG TBLs. Moreover, the shape factor curve in the high- Re wing is also below the ones at lower Re , which is associated with another effect of Reynolds number, *i.e.*, to reduce H .

We also analyzed, for $Re_c \geq 200,000$, the inner-scaled mean velocity profiles at $x_{ss}/c = 0.4$ and 0.7 , which are subjected to β values of 0.6 and 2 , respectively. For the three wing cases between $Re_c = 200,000$ and $1,000,000$, we compared the mean profiles with the ones from ZPG TBLs (Schlatter and Örlü, 2010) at approximately the same Re_τ . The ratios $\Phi_{U_e^+}$ and Φ_H have values larger than 1 (ranging from 1.07 and 1.23 , and from 1.05 and 1.16 , respectively), which is consistent with the features exhibited by APGs. Interestingly, both ratios decay with Re_c , which implies that low- Re TBLs are more sensitive to the effect of APGs, when exposed to the same $\beta(x)$ flow history. This conclusion is supported by the observations on several components of the Reynolds-stress tensor, in particular in the tangential velocity fluctuation profile and the Reynolds-shear stress. The values of the ratios $\Phi_{\bar{u}_t^2+}$ and $\Phi_{\bar{u}_t \bar{v}_n+}$ (which relate the APG and ZPG profiles with matched Re_τ , at $y_n/\delta_{99} = 0.2$) at $x_{ss}/c = 0.4$ and 0.7 are also larger than 1 , and range from 1.13 to 1.82 , and from 1.23 to 2.01 , respectively. Also in this case the ratios decrease with Re_c , which indicates that the outer region of the lower- Re wings is more energetic with respect to the corresponding ZPG than the higher- Re ; this also implies that the low- Re TBLs are more sensitive to APG effects. In fact, at $x_{ss}/c = 0.7$ the value of the \bar{u}_t^2+ profile at $y_n/\delta_{99} = 0.2$ is largest at $Re_c = 200,000$, and decays with increasing Re .

Our results show that two complementing mechanisms contribute to the development of the outer region in TBLs and the formation of large-scale en-

ergetic structures: one mechanism associated with the increase in Reynolds number, and another one connected to the APG. When the same streamwise evolution of the pressure-gradient magnitude is imposed, the low-Reynolds-number boundary layer becomes more severely affected by the APG, as also observed when analyzing the distributions of mean wall-normal velocity. In particular, the $Re_c = 200,000$ and $400,000$ wings exhibit V_e^+ values around 30% and 10% larger than those of the $1,000,000$, respectively, over a significant portion of the suction side of the wing. As illustrated in Figure 4, the APG increases wall-normal convection, which thickens the boundary layer allowing a larger outer region and leading to the formation of more energetic large-scale motions. These structures are taller, but shorter in the streamwise direction and more inclined with respect to the wall (Maciel et al., 2017), due to the increased V^+ . This suggests that a TBL at a higher Reynolds number, with a more “mature” outer region, is less affected by the effect of the APG. Further analyses of the current databases, with emphasis on extraction and characterization of coherent structures, will help to elucidate the differences in the mechanisms for outer-region energizing due to APG and Reynolds number.

Acknowledgments

The simulations were performed on resources provided by the Swedish National Infrastructure for Computing (SNIC) at the Center for Parallel Computers (PDC), in Stockholm (Sweden), and by the Partnership for Advanced Computing in Europe (PRACE) at the Barcelona Supercomputing Center (BSC) in Barcelona (Spain). RV and PS acknowledge the funding provided by the Swedish Research Council (VR) and from the Knut and Alice Wallenberg Foundation. This research is also supported by the ERC Grant No. “2015-AdG-694452, TRANSEP” to DH.

References

- Adrian, R. J., 2007. Hairpin vortex organization in wall turbulence. *Phys. Fluids* 19, 041301.
- Bobke, A., Vinuesa, R., Örlü, R., Schlatter, P., 2017. History effects and near-equilibrium in adverse-pressure-gradient turbulent boundary layers. *J. Fluid Mech.* 820, 667–692.

- Dixit, S. A., Ramesh, O. N., 2009. Determination of skin friction in strong pressure-gradient equilibrium and near-equilibrium turbulent boundary layers. *Exp. Fluids* 47, 1045–1058.
- Dong, S., Karniadakis, G. E., Chryssostomidis, C., 2014. A robust and accurate outflow boundary condition for incompressible flow simulations on severely-truncated unbounded domains. *J. Comput. Phys.* 261, 83–105.
- Eitel-Amor, G., Örlü, R., Schlatter, P., 2014. Simulation and validation of a spatially evolving turbulent boundary layer up to $Re_\theta = 8300$. *Int. J. Heat Fluid Flow* 47, 57–69.
- Fischer, P. F., Lottes, J. W., Kerkemeier, S. G., 2008. NEK5000: Open source spectral element CFD solver. Available at:
<http://nek5000.mcs.anl.gov>.
- Harun, Z., Monty, J. P., Mathis, R., Marusic, I., 2013. Pressure gradient effects on the large-scale structure of turbulent boundary layers. *J. Fluid Mech.* 715, 477–498.
- Hosseini, S. M., Vinuesa, R., Schlatter, P., Hanifi, A., Henningson, D. S., 2016. Direct numerical simulation of the flow around a wing section at moderate Reynolds number. *Int. J. Heat Fluid Flow* 61, 117–128.
- Hutchins, N., Marusic, I., 2007. Evidence of very long meandering features in the logarithmic region of turbulent boundary layers. *J. Fluid Mech.* 579, 1–28.
- Jansen, K., 1996. Large-eddy simulation of flow around a NACA 4412 airfoil using unstructured grids. In: Annual Research Briefs, 225–232.
- Jeong, J., Hussain, F., 1995. On the identification of a vortex. *J. Fluid Mech.* 285, 69–94.
- Jones, M. B., Marusic, I., Perry, A. E., 2001. Evolution and structure of sink-flow turbulent boundary layers. *J. Fluid Mech.* 428, 1–27.
- Kitsios, V., Atkinson, C., Sillero, J. A., Borrell, G., Gungor, A. G., Jiménez, J., Soria, J., 2016. Direct numerical simulation of a self-similar adverse pressure gradient turbulent boundary layer. *Int. J. Heat Fluid Flow* 61, 129–136.

- Lee, J. H., 2017. Large-scale motions in turbulent boundary layers subjected to adverse pressure gradients. *J. Fluid Mech.* 810, 323–361.
- Maciel, Y., Simens, M. P., Gungor, A. G., 2017. Coherent structures in a non-equilibrium large-velocity-defect turbulent boundary layer. *Flow Turbul. Combust.* 98, 1–20.
- Marusic, I., McKeon, B. J., Monkewitz, P. A., Nagib, H. M., Smits, A. J., Sreenivasan, K. R., 2010. Wall-bounded turbulent flows at high Reynolds numbers: recent advances and key issues. *Phys. Fluids* 22, 065103.
- Mellor, G. L., Gibson, D. M., 1966. Equilibrium turbulent boundary layers. *J. Fluid Mech.* 24, 225–253.
- Menter, F. R., 1994. Two-equation eddy-viscosity turbulence models for engineering applications. *AIAA J.* 32, 1598–1605.
- Monty, J. P., Harun, Z., Marusic, I., 2011. A parametric study of adverse pressure gradient turbulent boundary layers. *Int. J. Heat Fluid Flow* 32, 575–585.
- Negi, P. S., Vinuesa, R., Schlatter, P., Hanifi, A., Henningson, D. S., 2017. Unsteady aerodynamic effects in pitching airfoils studied through large-eddy simulations. In: *Int. Symp. Turbulence & Shear Flow Phenomena (TSFP-10)*, July 6–9, Chicago, US.
- Perry, A. E., Marusic, I., Jones, M. B., 2002. On the streamwise evolution of turbulent boundary layers in arbitrary pressure gradients. *J. Fluid Mech.* 461, 61–91.
- Pinkerton, R. M., 1938. The variation with Reynolds number of pressure distribution over an airfoil section. *NACA Annual Report* 24, 65–84.
- Rodríguez, I., Lehmkuhl, O., Borrell, R., Oliva, A., 2013. Direct numerical simulation of a NACA0012 in full stall. *Int. J. Heat Fluid Flow* 43, 194–203.
- Sanmiguel Vila, C., Örlü, R., Vinuesa, R., Schlatter, P., Ianiro, A., Discetti, S., 2017. Adverse-pressure-gradient effects on turbulent boundary layers: statistics and flow-field organization. *Flow Turbul. Combust.*, DOI 10.1007/s10494-017-9869-z.

- Sato, M., Asada, K., Nonomura, T., Kawai, S., Fuji, K., 2017. Large-eddy simulation of NACA 0015 airfoil flow at Reynolds number of 1.6×10^6 . *AIAA J.* 55, 673–679.
- Schlatter, P., Li, Q., Örlü, R., Hussain, F., Henningson, D. S., 2014. On the near-wall vortical structures at moderate Reynolds numbers. *Eur. J. Mech. B/Fluids* 48, 75.
- Schlatter, P., Örlü, R., 2010. Assessment of direct numerical simulation data of turbulent boundary layers. *J. Fluid Mech.* 659, 116–126.
- Schlatter, P., Örlü, R., 2012. Turbulent boundary layers at moderate Reynolds numbers: inflow length and tripping effects. *J. Fluid Mech.* 710, 5–34.
- Schlatter, P., Stolz, S., Kleiser, L., 2004. LES of transitional flows using the approximate deconvolution model. *Int. J. Heat Fluid Flow* 25, 549–558.
- Sillero, J. A., Jiménez, J., Moser, R. D., 2014. Two-point statistics for turbulent boundary layers and channels at Reynolds numbers up to $\delta^+ \approx 2000$. *Phys. Fluids* 26, 105109.
- Skote, M., Henningson, D. S., 2002. Direct numerical simulation of a separated turbulent boundary layer. *J. Fluid Mech.* 471, 107–136.
- Skåre, P. E., Krogstad, P.-r., 1994. A turbulent equilibrium boundary layer near separation. *J. Fluid Mech.* 272, 319–348.
- Spalart, P. R., Watmuff, J. H., 1993. Experimental and numerical study of a turbulent boundary layer with pressure gradients. *J. Fluid Mech.* 249, 337–371.
- Theodorsen, T., 1952. Mechanism of turbulence. In Proc. Second Midwestern Conference on Fluid Mechanics (Ohio State University, Columbus, OH).
- Townsend, A. A., 1956. The Structure of Turbulent Shear Flow. Cambridge Univ. Press, Cambridge, UK.
- Vinuesa, R., Bobke, A., Örlü, R., Schlatter, P., 2016a. On determining characteristic length scales in pressure-gradient turbulent boundary layers. *Phys. Fluids* 28, 055101.

- Vinuesa, R., Hosseini, S. M., Hanifi, A., Henningson, D. S., Schlatter, P., 2017a. Pressure-gradient turbulent boundary layers developing around a wing section. *Flow Turbul. Combust.*, DOI 10.1007/s10494-017-9840-z.
- Vinuesa, R., Negi, P. S., Hanifi, A., Henningson, D. S., Schlatter, P., 2017b. High-fidelity simulations of the flow around wings at high Reynolds numbers. In: *Int. Symp. Turbulence & Shear Flow Phenomena (TSFP-10)*, July 6–9, Chicago, US.
- Vinuesa, R., Örlü, R., Sanmiguel Vila, C., Iapiro, A., Discetti, S., Schlatter, P., 2017c. Revisiting history effects in adverse-pressure-gradient turbulent boundary layers. *Flow Turbul. Combust.*, DOI 10.1007/s10494-017-9845-7.
- Vinuesa, R., Prus, C., Schlatter, P., Nagib, H. M., 2016b. Convergence of numerical simulations of turbulent wall-bounded flows and mean cross-flow structure of rectangular ducts. *Meccanica* 51, 3025–3042.
- Vinuesa, R., Rozier, P. H., Schlatter, P., Nagib, H. M., 2014a. Experiments and computations of localized pressure gradients with different history effects. *AIAA J.* 55, 368–384.
- Vinuesa, R., Schlatter, P., 2017. Skin-friction control of the flow around a wing section through uniform blowing. In: *16th European Turbulence Conference (ETC)*, 21–24 August, Stockholm (Sweden).
- Vinuesa, R., Schlatter, P., Nagib, H. M., 2014b. Role of data uncertainties in identifying the logarithmic region of turbulent boundary layers. *Exp. Fluids* 55, 1751.
- Wolf, W. R., Azevedo, J. L. F., Lele, S. K., 2012. Convective effects and the role of quadrupole sources for aerofoil aeroacoustics. *J. Fluid Mech.* 708, 502–538.